Verification of a Complete Pore Network Simulator of Drainage and Imbibition

Tad W. Patzek, SPE, U. of California, Berkeley

Summary

Relative-permeability and capillary-pressure functions define how much oil can be recovered and at what rate. These functions, in turn, depend critically on the geometry and topology of the pore space, on the physical characteristics of the rock grains and the fluids, and on the conditions imposed by the recovery process. Therefore, imaging and characterizing the rock samples and the fluids can add crucial insight into the mechanisms that control field-scale oil recovery. When the fundamental equations of immiscible flow in the imaged samples are solved, one can elucidate how relative-permeability and capillary-pressure functions depend on wettability, interfacial tension, and the interplay among viscous, capillary and gravitational forces. This paper summarizes the development of a complete quasistatic pore-network simulator of two-phase flow, "ANetSim," and its validation against Statoil's state-of-the-art proprietary simulator. Most equations presented in this paper are new; therefore, repetition of the published Statoil results is kept to a minimum. In particular, the hydraulic conductance correlations in two-phase flow and the model of cooperative pore-body filling are new. ANetSim has been implemented in MATLAB® and it can run on any platform. Three-dimensional, disordered networks with complex pore geometry have been used to calculate primary-drainage and secondary-imbibition capillary pressures and relative permeabilities. The results presented here agree well with the Statoil simulations and experiments.

Introduction

The world works differently at different scales,[1] and earth sciences must therefore rely on different methods to model the diverse earth systems that range in size from atoms and molecules to the whole planet. **Fig. 1** shows the characteristic volume scales encountered in computational earth sciences, and **Fig. 2** shows the corresponding time scales. The respective scales of interest in this paper are highlighted. Both figures indicate the abundant interactions among the characteristic scales in earth sciences and the need for the appropriate computational tools. In particular, it is apparent that the molecular level approach, such as the Lattice-Gas or Boltzmann methods,[2] cannot be extended to describe rock cores, oil reservoirs, contaminant plumes, and the earth's crust. Conversely, a continuum description of a gas-condensate reservoir will fail to describe the motion of individual gas molecules that condense into thin films covering the rock surfaces.

At the bottom of Fig. 1, there are volume scales characteristic of individual molecules and thin films. The typical sizes of the pores of interest in this paper range from 1 μm in clays to 1 mm in coarse sandstones. One cubic centimeter of reservoir sandstone may have 200,000 pore bodies, 500,000 pore throats, and, when filled with two immiscible fluids, may contain some 2 million corner-filaments (also inappropriately called "corner films") of water in contact with the nonwetting fluid. A typical pore network consists of 10,000 to 20,000 pore bodies and pore throats, and has a volume of 0.1 cm^3 (10^{11} μm^3). Such a network is extracted from 3D microfocused X-ray computerized tomography (CT) images made of 30 to 1,000 mm^3 cubes or "voxels." Note that passing from the voxel to network description reduces the amount of information about the pore space by at least three orders of magnitude. A typical voxel in an aquifer or an oil reservoir is 0.001 to 10 m^3 (10^{15} to 10^{19} μm^3). Passing from a pore-network to a reservoir-voxel description reduces the amount of information about the pore space by an additional factor of 10^4–10^8. In contrast, a core voxel obtained from standard X-ray CT has a volume almost equal to a typical pore network. In fact, a large network with 500,000 pore bodies has been used recently to simulate corefloods in a heterogeneous carbonate.[3] This overlap establishes an important link between the pore-network models and the interpretation of coreflood results. A characteristic gridblock size in a field-scale flow simulation ranges from decimeters to hundreds of meters, causing yet another loss of information about the pore space. Oilfield interwell spacing ranges from tens of meters to several kilometers. We understand intuitively that "ghosts" of the pore structure should still be visible at the gridblock scale. The volume averaging methods that retain the shadows of the fine-scale structure are called *upscaling*.

The pore-network model presented in this paper is quasistatic and percolation description is appropriate. Percolation is about connectedness.[4] P.G. de Gennes, winner of the 1991 Nobel Prize in Physics for his seminal work on the theoretical physics of disordered materials, has described the percolation transition in the following way[5]: "Many phenomena are made of random islands and in certain conditions, among the islands, one macroscopic continent emerges."

Percolation phenomena are common in nature and occur in porous media (spontaneous imbibition without corner flow and with surface roughness), in multiphase systems (critical phenomena), in chemical systems (polymerization reactions), and in biological systems (the antibody-antigen immunological reactions). The special properties of a system, which emerge at the onset of macroscopic connectivity within it, are known as *percolation phenomena*.

In porous media, the invading fluid must be connected to the inlet to continue invading and the defending fluid must be connected to the outlet to be displaced. This dynamic percolation process is called *invasion percolation*.[6] If clusters of the defending fluid can become disconnected from the outlet, we call this process *percolation with trapping*.[7]

Primary drainage is a pure bond invasion-percolation problem, while imbibition is a problem in mixed invasion-percolation and ordinary percolation with trapping. The two processes are classified in **Fig. 3.** Previous studies (e.g., Refs. 8 and 9) have demonstrated that pore geometry determines which imbibition mechanisms occur, as seen in **Fig. 4.** Experiments show that both wetting and nonwetting fluids can flow simultaneously, but with different velocities, in the same pore. The wetting fluid remains in the extreme corners of the pore cross section and in the roughness of the walls. The existence of filament flow of wetting fluid explains the richness of mechanisms involved in imbibition.

This paper is structured as follows. First, the salient features of the pore-network description are discussed. Second, the pore-level description of drainage is summarized. Third, the imbibition mechanisms are discussed. Much of the pore-network description used in this paper follows that presented in Ref. 10. Here only the differences of approach will be highlighted, so as not to duplicate the work already presented by Øren *et al.*[10] The entire model presented in this paper has been described in detail elsewhere[11] and is a part of a graduate course at the U. of California, Berkeley, titled E240, "Fundamentals of Multiphase Flow in Porous Media."

This paper (SPE 71310) was revised for publication from paper SPE 59312, first presented at the 2000 SPE/DOE Improved Oil Recovery Symposium, Tulsa, Oklahoma, 3–5 April. Original manuscript received for review 13 April 2000. Revised manuscript received 1 January 2001. Manuscript peer approved 10 January 2001.

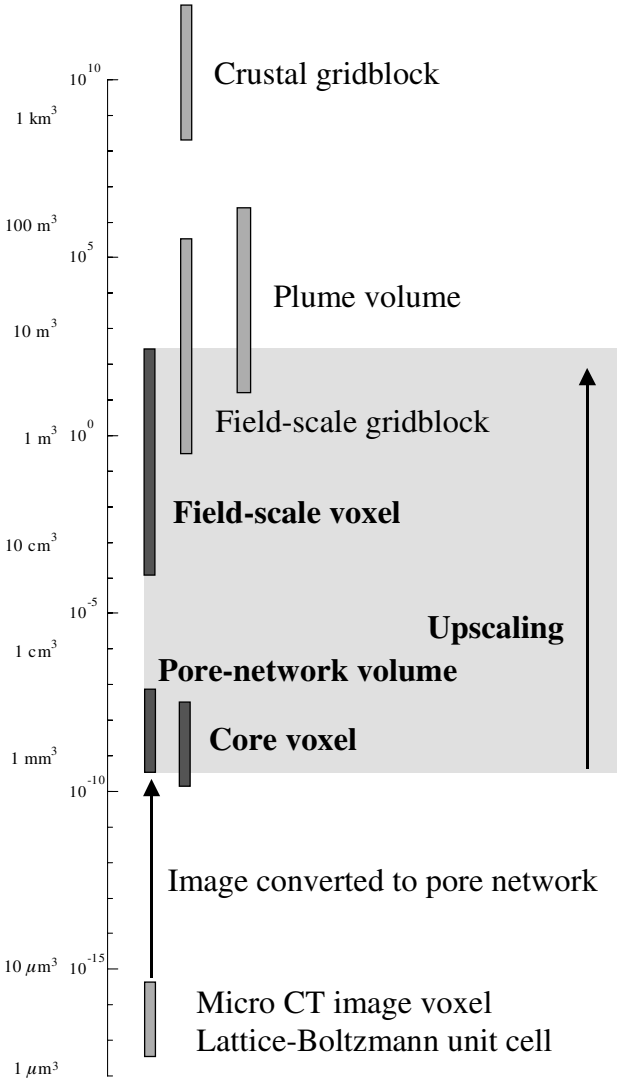

Fig. 1—Characteristic volume scales in earth sciences.

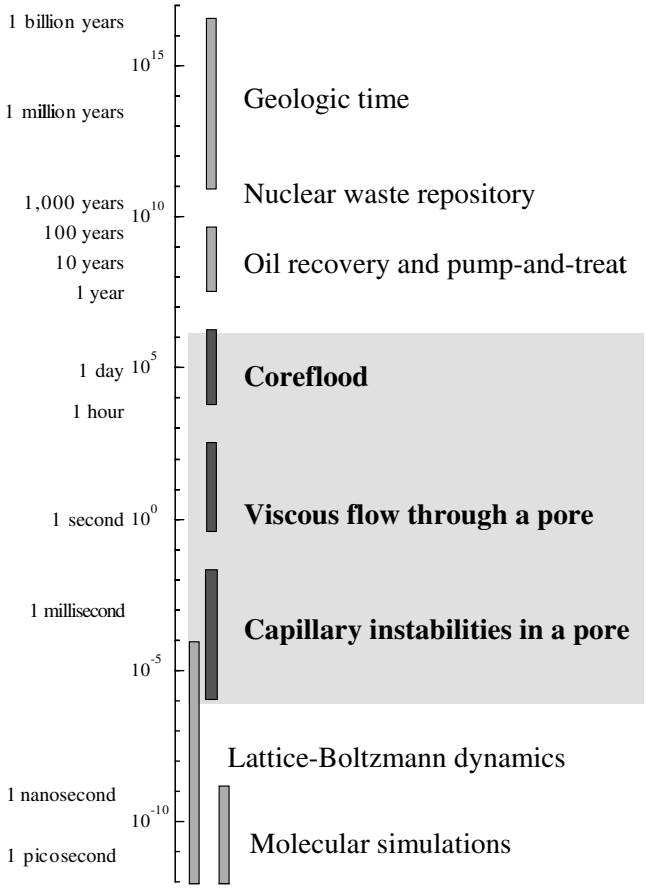

Fig. 2—Characteristic time scales in earth sciences.

Pore-Network Description

The 3D pore network used here is shown in **Fig. 5.** This network represents a 2.5-mm^3 sample of Bentheimer sandstone and consists of 3,677 pore bodies (nodes or sites) and 8,952 pore throats (links or bonds). The network connectivity varies, with 0 to 16 pore throats connected to a pore body. A uniform random distribution of receding (0.009 to 0.05°) and advancing (25 to 85°) contact angles is imposed. Most of the pores are triangular in

Flow type	Flow regime	Large/medium pores	Small pores
One-phase flow	Bulk flow	Effective medium approach	
Drainage	Bulk flow	Invasion percolation (IP)	
Imbibition	Bulk flow and corner flow	IP in dual network	Frontal drive compact growth
	Bulk flow and roughness flow	Bond percolation	Nucleation, compact cluster growth
Viscous flow	Stable	Flat interface	
	Unstable	Gradient governed growth or Diffusion limited aggregation (DLA)	

Fig. 3—Various pore-level displacement mechanisms and related statistical models (adapted from Ref. 9).

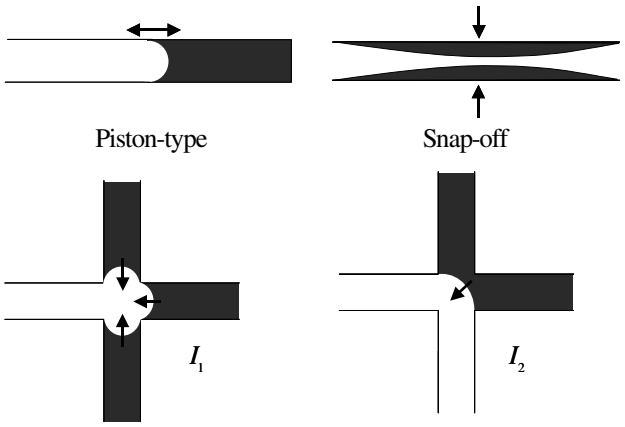

Fig. 4—Pore-level mechanisms in drainage (piston-type) and imbibition (all). I_1 and I_2 denote the cooperative pore-body filling with one- and two-pore throats filled with the nonwetting phase.

cross section and their shapes have been determined, albeit somewhat nonuniquely, from image analysis. There are 146 pore bodies that have square cross sections and 35 that are circular. There are 1,159 square pore throats and 789 that are circular. There are 183 pore bodies connected to the inlet and 208 connected to the outlet. The network porosity is 0.234, its microporosity is 0.014, and the absolute permeability is 5149 md (0.3% deviation relative to the Statoil calculation).

Pore Shapes. Real pore bodies and pore throats have complex and variable cross sections. Here we approximate them as cylindrical ducts of constant but arbitrary shapes of the cross sections. This means that all pores in the network are translationally symmetric along the cylinder generators. These cross sections and shapes are demonstrated in **Figs. 6 and 7.**

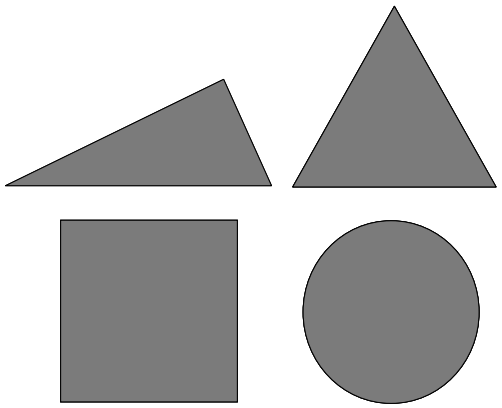

Fig. 6—Typical cross sections of flow ducts in the network.

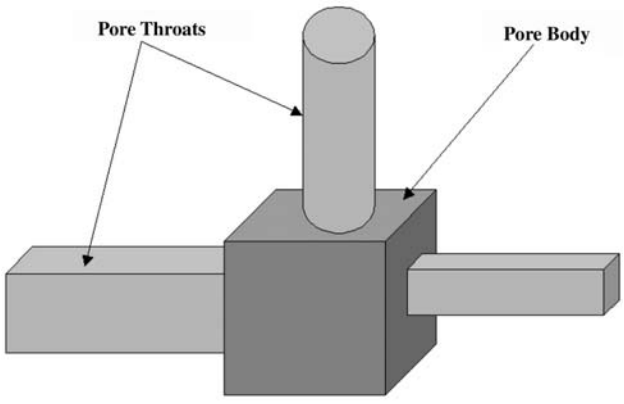

Fig. 7—The network is assembled by snapping together the individual "Lego" ducts.

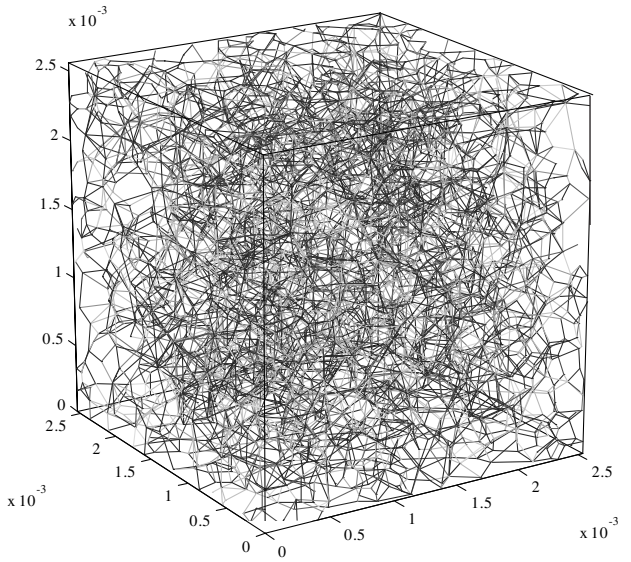

Fig. 5—3D network representation of a water-wet sandstone sample; the network description is courtesy of Statoil. The network dimensions are in meters.

The triangular-tube geometry is determined through two parameters: the shape factor, G, and the inscribed circle radius, r. Given the corner half-angles, $0 \le \beta_1 \le \beta_2 \le \beta_3 \le \pi/2$, we adopt a convention that β_1 and β_2 are the two corner half-angles subtended at the longest side of the triangle (its base). The pore cross-sectional area A and its perimeter P are expressed through Mason and Morrow's[12] "shape factor,"

$$G = \frac{A}{P^2} = \frac{1}{4\sum_{i=1}^{3} \cot \beta_i} = \frac{1}{4} \tan \beta_1 \tan \beta_2 \cot(\beta_1 + \beta_2), \quad \ldots\ldots (1)$$

which is the hydraulic radius of the pore made dimensionless by the perimeter P. For each G, only the triangular shapes between two limiting isosceles triangles, when $\beta_1 = \beta_2$ or $\beta_2 = \beta_3$, are admissible. The family of the limiting isosceles triangles is parameterized by the following angles:

$$\beta_{2,\min} = \beta_1 \text{ and } \beta_{2,\max} = \pi/4 - \beta_1/2. \quad \ldots\ldots\ldots\ldots\ldots\ldots (2)$$

Obviously, a single value of G corresponds to a range of corner half-angles and therefore triangular shapes **(Fig. 8).**

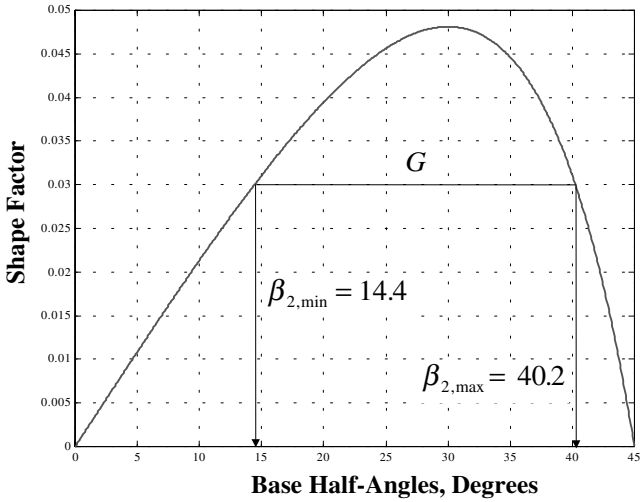

Fig. 8—The shape factor or "G-dome" vs. base half-angle ß2 for triangular pores. The feasible values of the shape factor and the base half-angles are inside the dome parameterized by Eq. 3. For equilateral triangles, $G = \sqrt{3}/36$, and the three real roots of Eq. 3 collapse to a single one at the dome peak.

Given the shape factor G of a triangular duct, the non-unique corner half-angles may be chosen as follows[13]:

- Find the bounds on β_2, $\beta_{2,\min} \le \beta_2 \le \beta_{2,\max}$, from Eqs. 4 and 5.
- Pick at random a value of $\beta_{2,\min} \le \beta_2 \le \beta_{2,\max}$.
- Use Eq. 6 to calculate the appropriate value of β_1.
- Calculate $\beta_3 = \pi/2 - \beta_1 - \beta_2$.

Using standard trigonometry, Eq. 1 is transformed to

$$t^3 - t + 8G = 0 \quad \ldots\ldots\ldots\ldots\ldots\ldots\ldots\ldots\ldots\ldots\ldots\ldots (3)$$

where $t \equiv \tan \beta_2$. The cubic Eq. 3 has three real roots for $0 < G < \sqrt{3}/36$. In particular, one can show[13]:

$$\beta_{2,\min} = \arctan\left\{\frac{2}{\sqrt{3}}\cos\left[\frac{\arccos\left(-12\sqrt{3}G\right)}{3} + \frac{4\pi}{3}\right]\right\}, \quad \ldots\ldots (4)$$

and

$$\beta_{2,\max} = \arctan\left\{\frac{2}{\sqrt{3}}\cos\left[\frac{\arccos\left(-12\sqrt{3}G\right)}{3}\right]\right\}. \quad \ldots\ldots\ldots (5)$$

Also, Eq. 1 can be solved for β_1 as a function of β_2:

$$\beta_1 = -\frac{1}{2}\beta_2 + \frac{1}{2}\arcsin\left(\frac{\tan\beta_2 + 4G}{\tan\beta_2 - 4G}\sin\beta_2\right). \quad \ldots\ldots\ldots (6)$$

Hydraulic Conductance. The unit-flow channel is shown in **Fig. 9.** In laminar flow of two immiscible phases, the flow rate of fluid i, water or oil, between two connected nodes I and J is given by:

$$q_{i,IJ} = \frac{g_{i,IJ}}{l_{IJ}}(p_{i,I} - p_{i,J}), \quad i = w, o, \quad \ldots\ldots\ldots\ldots\ldots (7)$$

where l_{IJ}=the spacing between the pore-body centers and $g_{i,IJ}$= the hydraulic conductance, m^4/Pa•s. To calculate the absolute permeability, we fill the network with a single fluid and index i disappears. We calculate the relative permeabilities of wetting and nonwetting phase by performing two separate calculations at several levels of capillary pressure (average wetting phase saturation). The first calculation is done for the wetting fluid, which spans the entire network, and the second one is restricted to the nodes and links invaded by the nonwetting fluid.

Flow resistances R_i add; therefore, the overall flow conductance is the harmonic mean of the conductances of the connecting throat and its two pore bodies:

$$R_{IJ} = R_t + \frac{1}{2}R_I + \frac{1}{2}R_J, \quad \ldots\ldots\ldots\ldots\ldots\ldots\ldots (8)$$

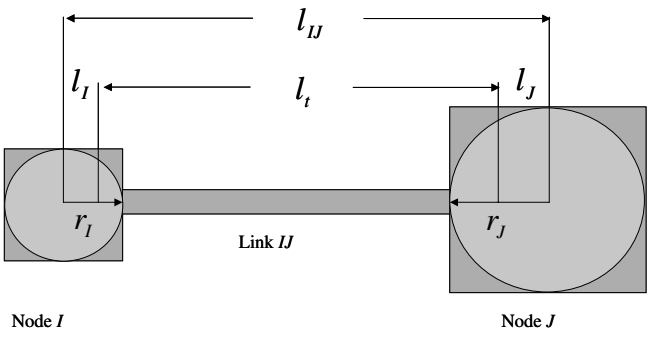

Fig. 9—Geometry of a unit-flow channel used to calculate the hydraulic conductance. The circles are cross sections of the largest spheres that can pass through each pore body; we call them the inscribed circles.

and

$$\frac{l_{IJ}}{g_{i,IJ}} = \frac{l_t}{g_{i,t}} + \frac{1}{2}\left(\frac{l_I}{g_{i,I}} + \frac{l_J}{g_{i,J}}\right) \quad i = w, o. \quad \ldots\ldots\ldots\ldots (9)$$

The factor of ½ enters because only one-half of each pore-body resistance is allocated to the unit-flow channel.

In steady-state flow of incompressible immiscible fluids, mass conservation in each pore body can be described through the vanishing sum of the volumetric flow rates:

$$\sum_{\substack{\text{All throats } K \\ \text{connected to body } I}} q_{i,IK} = 0, \quad i = w, o. \quad \ldots\ldots\ldots\ldots\ldots (10)$$

Eq. 7 can be inserted into Eq. 10 to yield a system of linear equations in the unknown node (pore-body) pressures. Dropping index i, the unknown pressures of the interior nodes are calculated from the following system of equations:

$$p_1\left(\sum_{K_1}\frac{g_{1,K_1}}{l_{1,K_1}}\right) - \sum_{K_1}\left(\frac{g_{1,K_1}}{l_{1,K_1}}\right)p_{K_1} = 0 \quad \ldots\ldots\ldots\ldots\ldots (11)$$

and

$$p_N\left(\sum_{K_N}\frac{g_{N,K_N}}{l_{N,K_N}}\right) - \sum_{K_N}\left(\frac{g_{N,K_N}}{l_{N,K_N}}\right)p_{K_N} = 0, \quad \ldots\ldots\ldots\ldots\ldots (12)$$

where N=the number of nodes.

Single-Phase Flow. The dimensionless hydraulic conductance of a duct with the equilateral triangle cross section may be calculated analytically, e.g.,[11,13]

$$\tilde{g}_{\max} = \frac{g\mu}{A^2} = \frac{3}{5}G_{\max}, \quad \ldots\ldots\ldots\ldots\ldots\ldots\ldots\ldots (13)$$

where $G_{\max} = \sqrt{3}/36$. Using conformal mapping[13] we demonstrate that Eq. 13 approximates the dimensionless hydraulic conductance of any triangular cross-sectional duct characterized by an arbitrary shape factor G **(Fig. 10):**

$$\tilde{g} = \frac{g\mu}{A^2} \approx \frac{3}{5}G\,. \quad \ldots\ldots\ldots\ldots\ldots\ldots\ldots\ldots (14)$$

The dimensionless conductances of the square and circular cross-sectional ducts are 0.5623 G and 0.5 G, respectively. **Fig. 11** shows the dimensionless hydraulic conductances in single-phase flow in triangular, rectangular, and elliptic ducts.

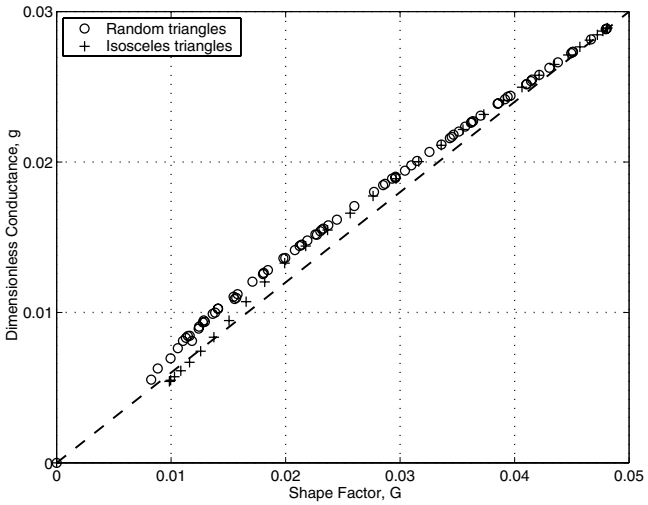

Fig. 10—Hydraulic-conductance-vs.-shape factor for an arbitrary triangular cross-sectional duct.[13]

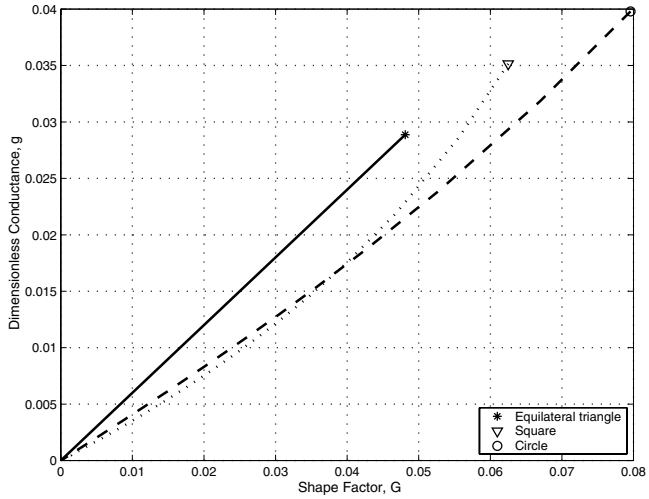

Fig. 11—The dimensionless hydraulic-conductance-vs.-shape factor for one-phase flow in the triangular, rectangular, and elliptic cross-sectional ducts. The markers denote the respective limiting values for an equilateral triangle, square, and circle.

Two-Phase Flow. When a nonwetting fluid is present, the wetting fluid forms cylindrical filaments along the corners of the duct, and is separated from the nonwetting fluid by translationally symmetric arc menisci (AM's). Here we assume that each AM surface is rigid and laden with surfactants, resulting in no-slip boundary conditions along the pore walls and the meniscus. The perfect slip and momentum continuity at the AM are described elsewhere.[14]

The Ransohoff-Radke Scaling. Our scaling of the Ransohoff-Radke finite element results is simpler than,[15] but essentially equivalent to, the two-phase hydraulic conductance correlations used by Statoil.[10] The conductance, $g_{w,i}$, of an angular pore with wetting-liquid filament in corner i is[15]:

$$g_{w,i} = \frac{r_w^2 A_{w,i}}{\chi_{w,i}\mu_w}, \quad \ldots\ldots\ldots\ldots\ldots\ldots\ldots\ldots\ldots\ldots (15)$$

where $r_w = \gamma/P_c$ the radius of curvature of the filament set by the prevailing capillary pressure, P_c, and the interfacial tension, γ; $A_{w,i}$ = the cross-sectional area of filament flow; $\chi_{w,i}$ = the Ransohoff-Radke dimensionless resistance factor; and μ_w = the bulk viscosity of wetting liquid.

By inspection, it follows from Eq. 15 that when the sum of corner half-angle, β_i, and contact angle, θ, approaches the limit of flat interface,

$$\lim_{\theta\to\theta^*} \theta + \beta_i = \pi/2, \quad \ldots\ldots\ldots\ldots\ldots\ldots\ldots\ldots\ldots\ldots (16)$$

capillary pressure goes to zero and both the radius of interface curvature, r_w, and the resistance factor, $\chi_{w,i}$, go to infinity.

From the numerical solution, it follows that the resistance factor goes to infinity exponentially as the contact angle approaches the limit of θ^*. Hence, it can be argued that, at least close to that limit, the resistance factor scales as

$$\chi \propto \exp\left(\frac{\theta}{\theta^* - \theta}\right) \quad \ldots\ldots\ldots\ldots\ldots\ldots\ldots\ldots\ldots\ldots (17)$$

or in $\chi(\theta^* - \theta) \propto \theta$. $\ldots\ldots\ldots\ldots\ldots\ldots\ldots\ldots\ldots\ldots (18)$

If scaling (Eq. 18) is universal, then it also follows that

$$\text{In}\ \chi(\theta^* - \theta) = \alpha(\theta^*) + \delta(\theta^*)\frac{\theta}{\theta^*} \quad \ldots\ldots\ldots\ldots\ldots\ldots\ldots\ldots (19)$$

where α and δ = the constants that depend only on the limiting contact angle, and the ratio θ^*/θ is the appropriate stretching transformation. It also follows that in the limit of $\theta \to \theta^*$, the left side of Eq. 19 is a constant; therefore,

$$\alpha(\theta^*) + \delta(\theta^*) = \text{const}, \quad \ldots\ldots\ldots\ldots\ldots\ldots\ldots\ldots\ldots\ldots (20)$$

is an invariant of the scaling above. In other words, all resistance factors are the same at $\theta = \theta^*$ when represented by Eq. 19. This is because the singularity in χ is caused only by the approach to θ^* but it does not depend on a particular value of θ^*.

Armed with this knowledge, we may now begin to analyze the numerical solutions of Ransohoff and Radke, bearing in mind that in the limit of $\theta \to \theta^*$ their solutions will suffer from a severe loss of accuracy. This is because near the asymptote, small numerical errors in the determination of average liquid velocity and in meniscus radius are amplified exponentially when χ is calculated.

The 30° and 45° corner half-angles are the only ones for which the numerical solutions have been published as a function of contact angle. Our goal, however, is to calculate the resistance factor for an arbitrary corner half-angle and arbitrary contact angles. Here the scaling invariant Eq. 18 becomes helpful. For the zero contact angle, Ransohoff and Radke have tabulated the numerical results for seven corner half-angles, including 30° and 45° degrees. In other words, they have allowed us to approximate the function $\alpha(\theta^*)$ and, thus, $\delta(\theta^*)$ as these two functions add up to a constant. For the infinite surface viscosity, a single parabola fits all the available $\delta(\theta^*)$ very well:

$$\begin{aligned}\alpha(\theta^*) &= \alpha_1\theta^{*2} + \alpha_2\theta^* + \alpha_3 \\ &= -3.76219\theta^{*2} + 7.07451\theta^* + 1.09774\end{aligned}, \quad \ldots\ldots\ldots\ldots (21)$$

Then

$$\begin{aligned}\delta(\theta^*) &= \alpha_1\theta^{*2} - \alpha_2\theta^* + (\alpha_3 + 0.505494) \\ &= -3.76219\theta^{*2} + 7.07451\theta^* - 0.592246\end{aligned}, \quad \ldots\ldots\ldots\ldots (22)$$

where 0.505494 = the invariant (Eq. 20) obtained from the two numerical solutions at $\theta^* = 1$.

The final functional form of the dimensionless resistance factor in the corner filament flow of wetting liquid is therefore

$$\chi(\beta,\theta) = \exp\left[\frac{\alpha(\theta^*) + \delta(\theta^*)\dfrac{\theta}{\theta^*}}{(\theta^* - \theta)}\right], \quad \ldots\ldots\ldots\ldots\ldots\ldots (23)$$

$$\theta^* = \pi/2 - \beta,\ \theta < \theta^*, \quad \ldots\ldots\ldots\ldots\ldots\ldots\ldots\ldots\ldots\ldots (24)$$

where all the angles are expressed in radians and α and δ are given by Eqs. 21 and 22.

The symmetry of expression (Eqs. 23 and 24) about the asymptote $\theta = \theta^*$ suggests that the same expression should hold when $\theta > \theta^*$ if the denominator in the exponent is replaced with $\theta - \theta^*$ and θ/θ^* is remapped from the interval $[0,\theta^*$ to the interval $\theta^*, \pi]$:

$$\chi(\beta,\theta) = \exp\left[\frac{\alpha(\theta^*) + \delta(\theta^*)\dfrac{\pi - \theta}{\pi - \theta^*}}{(\theta - \theta^*)}\right], \quad \ldots\ldots\ldots\ldots\ldots\ldots (25)$$

$$\theta^* = \pi/2 - \beta,\ \theta > \theta^*, \quad \ldots\ldots\ldots\ldots\ldots\ldots\ldots\ldots\ldots\ldots (26)$$

The Patzek-Kristensen Scaling[14]

Our scaling (Eqs. 23 through 26) agrees with the Ransohoff-Radke finite-element solutions to within a factor of two, as seen in **Fig. 12.** It now appears that we can do much better than that.

The dimensionless conductance of wetting fluid is defined as $\tilde{g}_w = g_w\mu_w/b^4$, where b = the meniscus-apex distance along the wall. The dimensionless corner-flow conductances have been calculated elsewhere[14,16] for a variety of corner half-angles and contact angles

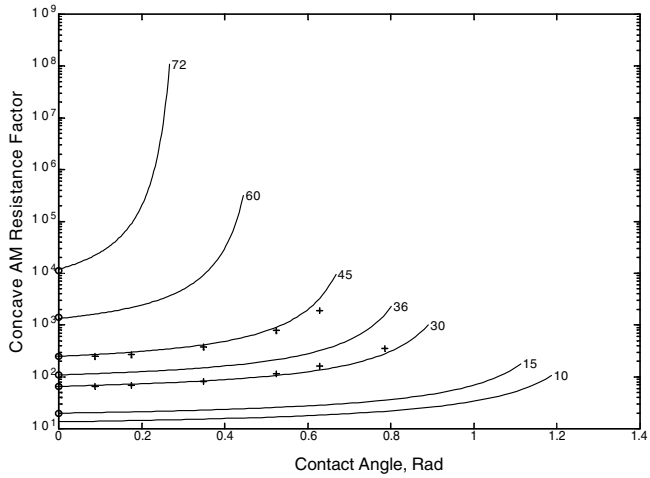

Fig. 12—Plot of the dimensionless resistance factors for the infinite surface viscosity vs. the contact angle. The arc menisci are concave and become flat only asymptotically. All available numerical solutions are shown. The circles denote the zero-contact angle FE solutions in Ref. 15, and the crosses depict the 30° and 45° corner half-angle solutions. The labels denote the corner half-angles in degrees. The crosses highlight gradual loss of accuracy of the numerically determined resistance factors near the respective asymptotes.

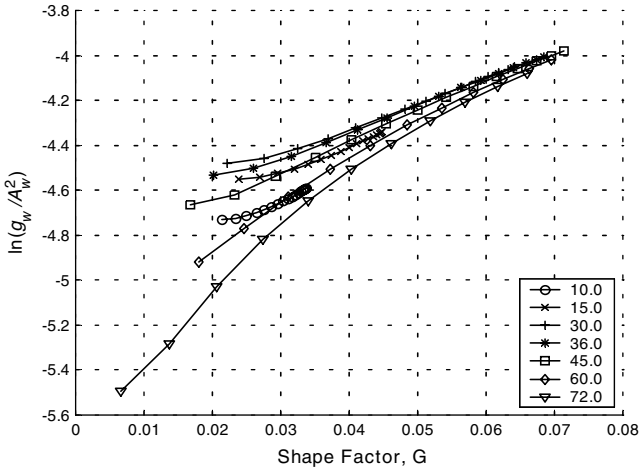

Fig. 13—The logarithm of the ratio of the dimensionless hydraulic conductance and the dimensionless corner filament area squared vs. the filament shape factor for corner half angles between 10 and 72°.

(Fig. 13), using a high-resolution finite-element method implemented in MATLAB.[17]

With $b=1$, the dimensionless flow cross-sectional area and shape factor of the single corner filament are calculated as follows:

$$\tilde{A}_w = \begin{cases} \sin\beta\cos\beta, & \text{if } \theta+\beta=\pi/2 \\ \left[\frac{\sin\beta}{\cos(\theta+\beta)}\right]^2\left[\frac{\cos\theta\cos(\theta+\beta)}{\sin\beta}+\theta+\beta-\frac{\pi}{2}\right], \end{cases} \quad \ldots\ldots\ldots\ldots\ldots\ldots\ldots (27)$$

otherwise

$$\tilde{G} = \begin{cases} \dfrac{\tilde{A}_w}{4(1+\sin\beta)^2}, & \text{if } \theta+\beta=\pi/2 \\ \dfrac{\tilde{A}_w}{4\left[1-\sin\beta/\cos(\theta+\beta)(\theta+\beta-\pi/2)\right]^2} \end{cases} . \quad \ldots\ldots\ldots (28)$$

The dimensional hydraulic conductance in corner-flow of the wetting phase is obtained by multiplying $\tilde{g}_w$ with the corresponding $2b^4/\mu_w$ (the dimensionless conductance was calculated for half of the meniscus area, hence the factor of two).

We propose[14] to scale the dimensionless hydraulic conductance of the corner wetting phase filaments as follows:

$$\tilde{g}_w = \ln\left(\frac{\tilde{g}_w}{\tilde{A}_w^2}\right)\left(\frac{1}{4\pi}-\tilde{G}\right)^{e_1}\cos^{e_2}\left(\beta-\frac{\pi}{6}\right) - 0.02\sin\left(\beta-\frac{\pi}{6}\right) \quad \ldots\ldots\ldots\ldots\ldots\ldots\ldots (29)$$

where $e_1=7/8$ and $e_1=1/2$ for the no-slip boundary condition at the water/oil interface. Eq. 29 yields a universal curve when plotted vs. shape factor, as shown in **Fig. 14.**

The structure of scaling in Eq. 29 can be explained as follows. All curves in Fig. 13 converge as the shape factor approaches that of circle, $G=1/4\pi\approx 0.08$. Hence, the middle factor in the first term on the right side of Eq. 29 compensates for the deviation of shape factor from that of a circle. The third factor in the first term in Eq. 29 compensates for the deviation of corner geometry from that of an equilateral triangle corner. In Fig. 13, the curves for the 45°- and 15° corner half-angles are close to each other, as are those for the 60°- and 10° corner half-angles. The last term on the right side of Eq. 29 moves the $\beta=72°$ corner half-angle points onto the universal curve.

For each corner half-angle, the scaling in Eq. 29 produces an almost straight line. The slopes of the respective lines and their intercepts are very similar and, in turn, can be summarized as a quadratic function of shape function[14]:

$$\tilde{g}_w = a_1\tilde{G}^2 + a_2\tilde{G} + a_3, \quad \ldots\ldots\ldots\ldots\ldots\ldots\ldots\ldots (30)$$

and $a_1=-15.1794$, $a_2=7.6307$, $a_3=-0.53488$. $\ldots\ldots\ldots\ldots (31)$

For perfect slip at the water/oil interface, the exponents are $e_1=1$ and $e_2=0$, and[14]:

$$\tilde{g}_w = a_1\tilde{G}^2 + a_2\tilde{G} + a_3, \quad \ldots\ldots\ldots\ldots\ldots\ldots\ldots\ldots (32)$$

and $a_1=-18.2066$, $a_2=5.88287$, $a_3=-0.351809$. $\ldots\ldots\ldots (33)$

The dimensional hydraulic conductance in the corner flow of the wetting phase is obtained by multiplying $\tilde{g}_w$ with the corresponding b^4/μ_w.

Eq. 29 is compared with the finite-element results in **Fig. 15.** The mean absolute relative error of the approximation is 6.2%; however, for wide corner half-angles, 60° and 72°, and large contact angles, the relative error is larger **(Fig. 16).** Because the overall hydraulic conductance of wetting fluid is limited by the lowest

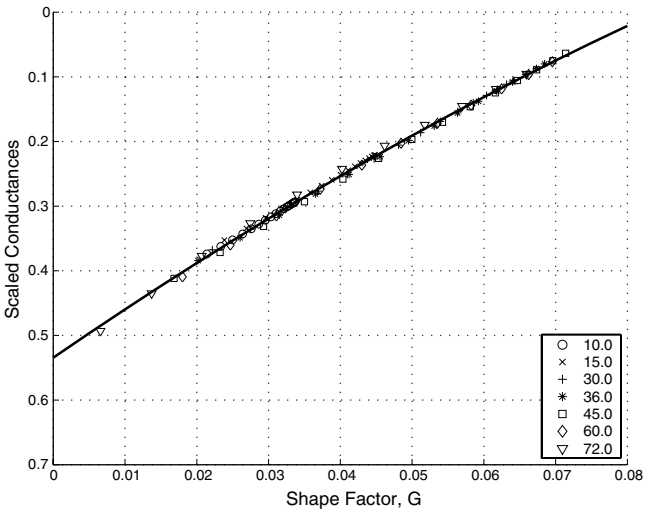

Fig. 14—The scaled hydraulic conductance, Eq. 29, vs. shape factor.

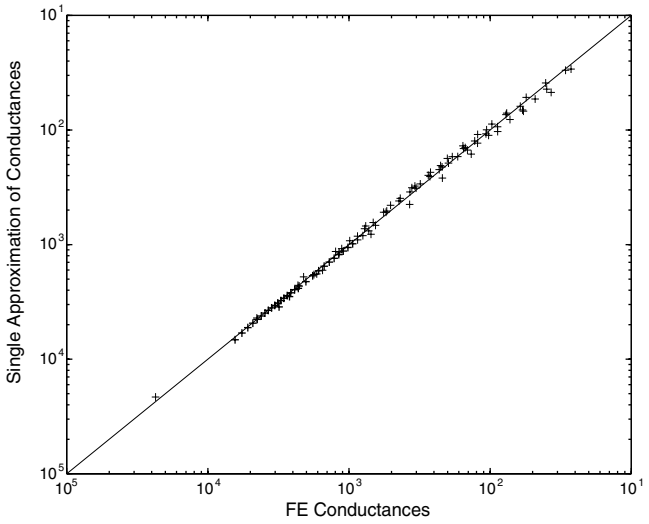

Fig. 15—Approximation in Eq. 29 vs. the finite element (FE) results for the no-slip case.

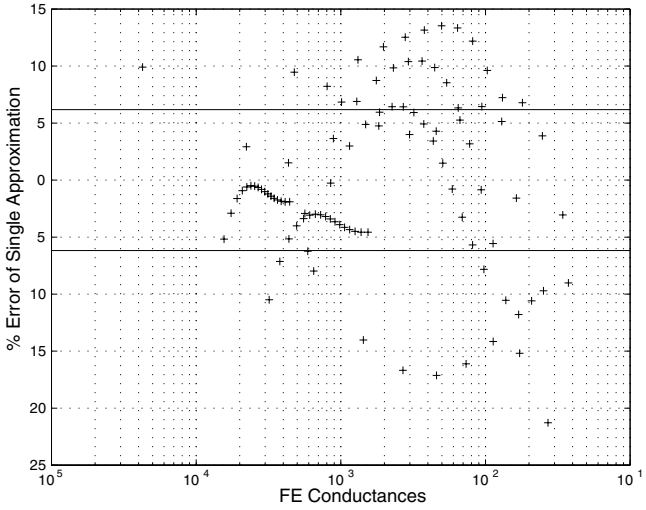

Fig. 16—Percent relative error of the approximation in Eq. 29 increases for large corner half-angles and large contact angles. The horizontal lines denote the mean absolute error.

individual filament conductances, the decreasing accuracy of the simple approximation given by Eq. 25 is acceptable.

Drainage

We follow Øren *et al.*'s[10] generalization of Mason and Morrow's[12] expression for the threshold capillary entry-pressure in drainage. The receding contact-angle and the triangular pore shape are arbitrary. The Mayer-Stowe-Princen (MSP) method for calculating the threshold pressure relies on equating the curvature of the corner AM's to the curvature of the invading interface.[18–21] The pore-volume work of displacing water from a pore translates into the threshold capillary entry-pressure, which is inversely proportional to the inscribed circle radius, and depends on the contact angle and pore shape. Piston-type drainage of a triangular pore is shown in **Fig. 17,** when there is no contact-angle hysteresis, and the capillary pressures are made dimensionless with the inscribed circle radius and interfacial tension. Drainage is a bond invasion-percolation process. Therefore, the calculations are performed in order of increasing threshold capillary entry-pressures; only the accessible pore throats and their pore bodies are invaded at each step.

The threshold capillary entry-pressure in primary drainage in a triangular pore can be expressed as

$$P^{e}_{c,PD} = \frac{\gamma}{r_d} = \frac{\gamma}{r}\cos\theta_r(1+2\sqrt{\pi G})F_d(\theta_r, G, C_1), \quad \ldots\ldots\ldots (34)$$

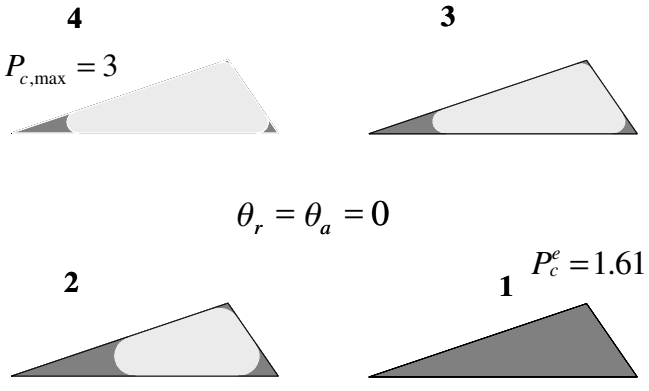

Fig. 17—Piston-type drainage (1,2,3,4) or imbibition (4,3,2,1) without contact-angle hysteresis in a triangular pore, G=0.01. Four frames from a single-pore mechanisms visualization simulator, "AMSim"24 are shown. The dimensionless capillary entry pressure is 1.61, and the maximum capillary pressure in drainage is 3.

where γ=the interfacial tension, r=the inscribed circle radius, and

$$F_d(\theta_r, G, C_1) = \frac{1+\sqrt{1-4GC_1/\cos^2\theta_r}}{(1+2\sqrt{\pi G})}, \quad \ldots\ldots\ldots\ldots (35)$$

is a function of the corner half-angles through

$$C_1 = \sum_{i=1}^{3}\left[\cos\theta_r\frac{\cos(\theta_r+\beta_i)}{\sin\beta_i} - \left(\frac{\pi}{2}-\theta-\beta_i\right)\right]. \quad \ldots\ldots\ldots (36)$$

C_1 is not universal for a given G if the AM's are not present in all pore corners. Note that $F_d(\theta_r=0,G,C_1)=1$, regardless of how many pore corners have the water AM. Also note that a similar expression in Ref. 10 depends on another constant, D, which is a combination of three constants.

Drainage Results. Primary drainage of the sandstone network in Fig. 5 is shown in **Fig. 18.** ANetSim calculations compare very well with the Statoil model. The drainage relative-permeability curves are shown in **Fig. 19.** The slight discrepancies between ANetSim and the Statoil simulator are most pronounced at inter-

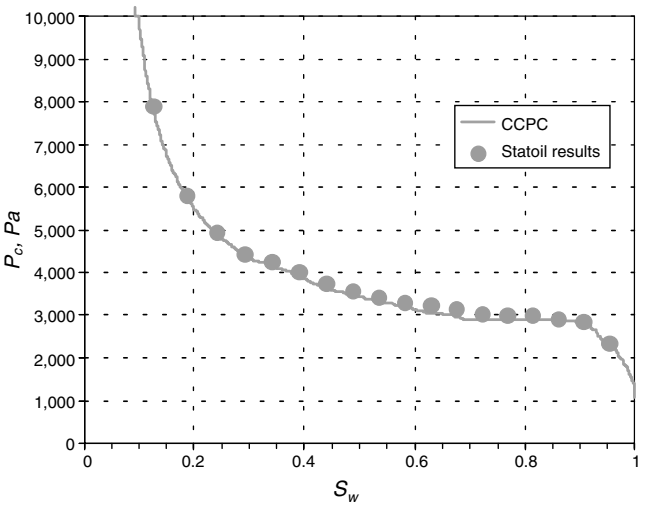

Fig. 18—The calculated capillary-pressure curve in primary drainage of the Bentheimer sandstone network vs. the Statoil results (circles) from P.-E. Øren, *et al.*

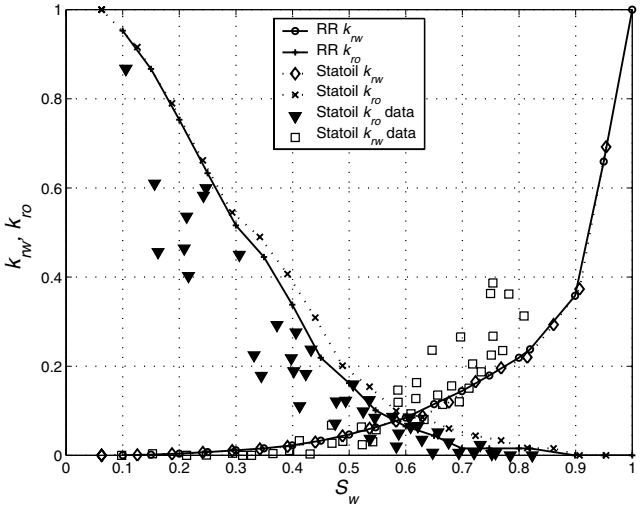

Fig. 19—The relative-permeability curves in primary drainage of the Bentheimer sandstone network vs. the Statoil calculations and experiments (Ref. 10, their Fig. 14). Note that k_{ro} calculated by ANetSim better fits the experimental data.

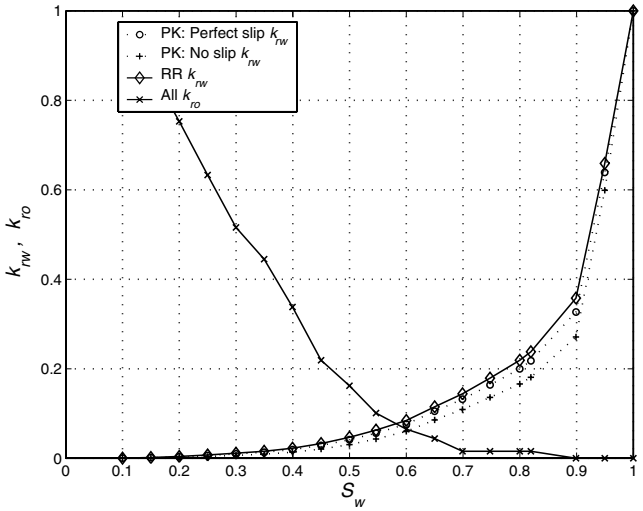

Fig. 20—Comparison of the calculated-drainage relative permeabilities of the Bentheimer sandstone network. The Patzek-Kristensen (PK) scaling with no slip at the water/oil interfaces results in a k_{rw} that is practically the same as the asymptotic scaling of the Ransohoff-Radke (RR) calculations, Eq. 21. The PK scaling with perfect slip at the water/oil interfaces results in a consistently lower k_{rw}. All three k_{ro}'s are the same.

mediate oil saturations as shown in **Figs. 20 and 21.** These discrepancies may be caused by subtle differences in the invasion-percolation algorithms and by different precision of the respective calculations (64 bits for ANetSim and 128 bits for Statoil).

Imbibition

The microscopic picture of imbibition in porous media is much more complicated than that of drainage (see Refs. 10 and 11). Imbibition with trapping is a special case of bond-and-site invasion percolation, in which the nonwetting fluid clusters must be connected to the outlet. Imbibition is very slow and the invading wetting fluid spans the entire medium through corner filaments. In contrast, the clusters of nonwetting fluid become trapped when their escape paths are cut off by the bond-breaking mechanisms.

As capillary pressure decreases, the pore throats fill in order of increasing radius, with the narrowest filling first. The throat filling starts by snap-off [if initially there are no main terminal arc menisci (MTAM)], and then by piston-type imbibition. These two mechanisms can be described by ordinary bond percolation on a dual network and bond-invasion percolation.[9] At the same time, the pore bodies attached to the invaded throats are subject to cooperative pore-body filling by the I_n events. The latter mechanism and snap-off generate compact clusters of wetting fluid. The frequency of events during imbibition of the network in Fig. 5 is shown in **Fig. 22.**

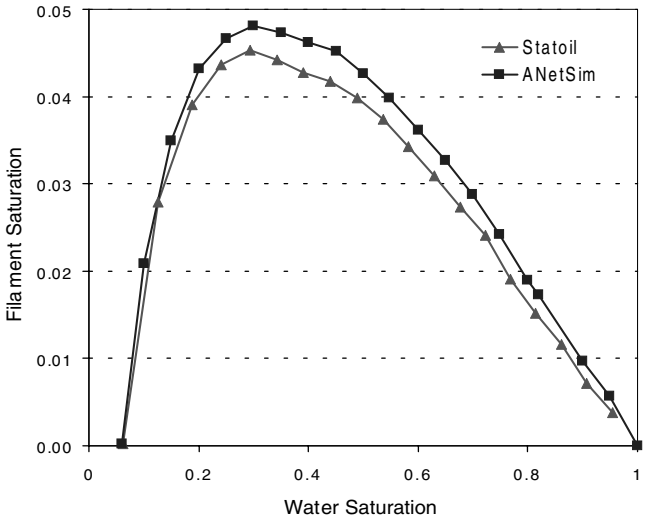

Fig. 21—The overall saturation of corner filaments vs. average water saturation in drainage of the Bentheimer sandstone network. Note that at intermediate water saturations, ANetSim predicts consistently higher filament saturations.

Piston-Type Imbibition. If there is contact-angle hysteresis, $\theta_a > \theta_r$, each corner AM hinges about its contact line, pinned at a distance b_i from the corner apex, until the hinging contact angle, $\theta_{h,i}$, exceeds the advancing contact angle, θ_a. Thereafter, the AM slides at the advancing contact angle while decreasing its radius of curvature, r_p, to accommodate the current capillary pressure in imbibition. The AM in the sharpest corner slides first while the AM in the widest corner slides last. The pinned AM's decrease their curvature simply by swelling. The final capillary pressure in primary drainage determines the smallest radius of menisci curvature, $r_{pd}=\gamma/P_{c,\max}$.

The maximum advancing contact angle at which spontaneous piston-type imbibition can occur is defined by the requirement that the effective perimeter wetted by oil be zero:

$$\cos\theta_{a,\max} \approx \frac{-4G\sum_{i=1}^{3}\cos(\theta_r+\beta_i)}{P_{c,\max}r/\gamma-\cos\theta_r+12G\sin\theta_r}, \quad \ldots\ldots\ldots\ldots (37)$$

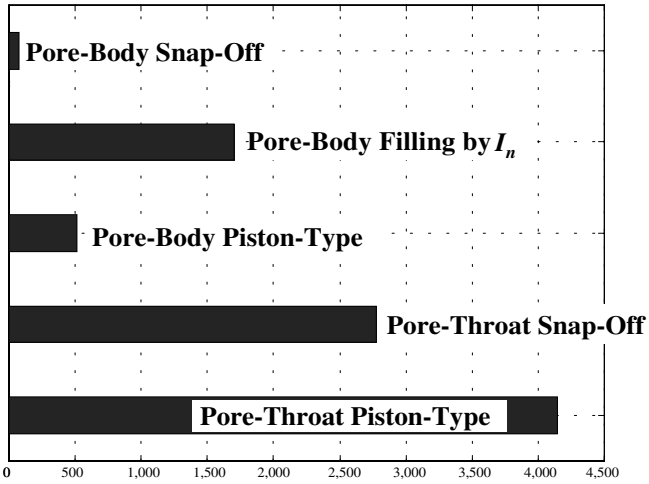

Fig. 22—The numbers of pore-level events during imbibition of the Bentheimer sandstone network.

and it depends on the pore geometry, receding contact angle, and the maximum capillary pressure in primary drainage.

In a triangular pore, the threshold capillary pressure in spontaneous imbibition (i.e., for $\theta_a \le \theta_{a,\max}$), with contact-angle hysteresis, can be calculated by solving the following system of seven nonlinear algebraic equations in $\theta_{h,i}$, α_i, i=1,2,3 and r_p:

$$\theta_{h,i} = \min\left\{\arccos\left[\frac{r_{pd}}{r_p}\cos(\theta_r+\beta_i)\right]-\beta_i, \theta_a\right\} \quad i=1,\ 2,\ 3; \quad \ldots\ldots\ldots\ldots\ldots\ldots\ldots (38)$$

$$b_i = \begin{cases} r_{pd}\dfrac{\cos(\theta_r+\beta_i)}{\sin\beta_i}, & \text{if } \theta_{h,i} \le \theta_a \\ r_p\dfrac{\cos(\theta_a+\beta_i)}{\sin\beta_i}, & \text{if } \theta_{h,i} > \theta_a \end{cases} \quad i=1,\ 2,\ 3; \quad \ldots\ldots\ldots (39)$$

$$\alpha_i = \begin{cases} \arcsin\left(\dfrac{b_i}{r_p}\sin\beta_i\right), & \text{if } \theta_{h,i} \le \theta_a \\ \pi/2-\theta_a-\beta_i, & \text{if } \theta_{h,i} > \theta_a \end{cases} \quad i=1,\ 2,\ 3; \quad \ldots\ldots\ldots (40)$$

and

$$r_p = \frac{\dfrac{r^2}{4G} - r_p\sum_{i=1}^{3} b_i\cos\theta_{h,i} + r_p^2\sum_{i=1}^{3}\left(\dfrac{\pi}{2}-\theta_{h,i}-\beta_i\right)}{2r_p\sum_{i=1}^{3}\alpha_i + \left(\dfrac{r}{2G}-2\sum_{i=1}^{3} b_i\right)\cos\theta_a}. \quad \ldots\ldots\ldots (41)$$

The threshold capillary pressure in piston-type imbibition is then $P_{c,PT}^e = \gamma / r_p$.

If contact-angle hysteresis is too large, the corner menisci remain pinned, while the MTAM is forced into the pore at a negative capillary pressure, as in primary drainage. When $\theta_a \ge \pi/2+\max(\beta_i)$, imbibition is forced and intermediate oil filaments may be created if the maximum capillary pressure in drainage is high enough **(Fig. 23).** In this case, the threshold capillary pressure in piston-type imbibition is obtained from Eq. 34 with θ_r replaced with θ_a.

When $\theta_{a,\max} < \theta_a < \pi/2+\max(\beta_i)$, geometry prevents the creation of intermediate films and the MTAM is forced into the pore when each of its radii of curvature equals $r/\cos\theta_a$:

$$P_{c,PT}^e = \frac{2\gamma\cos\theta_a}{r}. \quad \ldots\ldots\ldots\ldots\ldots\ldots\ldots\ldots (42)$$

Note that in piston-type drainage and imbibition, each pore behaves as a highly nonlinear valve with threshold and hysteresis that is proportional to the contact-angle hysteresis, as in **Fig. 24.**

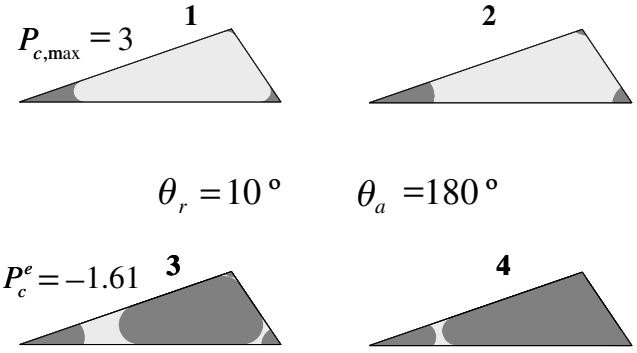

Fig. 23—Piston-type imbibition with extreme contact-angle hysteresis. When the MTAM invades, oil films are created and ultimately squeezed out of the pore.

Cooperative Pore-Body Filling. The largest radius of curvature of a water/oil interface in a pore body and its oil-filled pore throats defines the threshold capillary pressure necessary to fill that pore body. Thus, this threshold pressure never exceeds that of piston-type invasion of a connecting pore throat filled with oil. The required radius of curvature depends on the size of the pore body and on the number and spatial distribution of connecting pore throats filled with oil. For a pore body with a coordination number z, there are z-1 such pore-body filling mechanisms, as seen in Fig. 4. We refer to them as I_1 through I_{z-1}. If only one of the connecting throats contains oil (i.e., the mechanism is I_1), the pore-body filling is similar to that of a piston-type invasion described above and the threshold pressure is almost the same.

The threshold pressure for the I_2 to I_{z-1} mechanisms are more complex. Blunt[22] has presented a parametric model for these mechanisms. If $\theta_a < \theta_{a,\max}$, the mean radius of curvature for filling by an I_n mechanism is calculated as:

$$\overline{R}_n = \frac{1}{\cos\theta_a}\left(r_0 + \sum_{i=1}^{n} a_i r_i x_i\right), \quad \ldots\ldots\ldots\ldots\ldots\ldots (42)$$

where r_0=the pore body radius, r_i=the radii of the oil-filled pore throats, a_i=geometrical constants, and x_i=random numbers between zero and one. The threshold pore-filling capillary pressure for the I_n mechanism is then

$$P_{c,n}^e = \frac{2\gamma}{\overline{R}_n}. \quad \ldots\ldots\ldots\ldots\ldots\ldots\ldots\ldots\ldots (44)$$

Improving on this idea, we propose the following model of cooperative pore-body filling. For an I_2 event, the effective radius of curvature is equal to

$$\overline{R}_2 = \left[r_0 + w_1^{(2)} r_1 + w_2^{(2)} r_2\right]/\cos\theta_a \quad \ldots\ldots\ldots\ldots\ldots\ldots (45)$$

where r_0=the pore body radius, r_1 and r_2=the radii of the oil-filled pore throats that participate in the event, and $w_1^{(2)}$ and $w_2^{(2)}$=the throat radii weights for the I_2 event. These weights in principle could be calculated from the geometry of the pore body and the pore throats involved in a particular I_2 event. Because we do not know this geometry exactly, we may assume that

$$\overline{R}_2 = [r_0 + w_{1,2}^{(2)}(r_1+r_2)]/\cos\theta_a \quad \ldots\ldots\ldots\ldots\ldots\ldots (46)$$

Eq. 46 still requires us to recalculate the effective radius of curva-

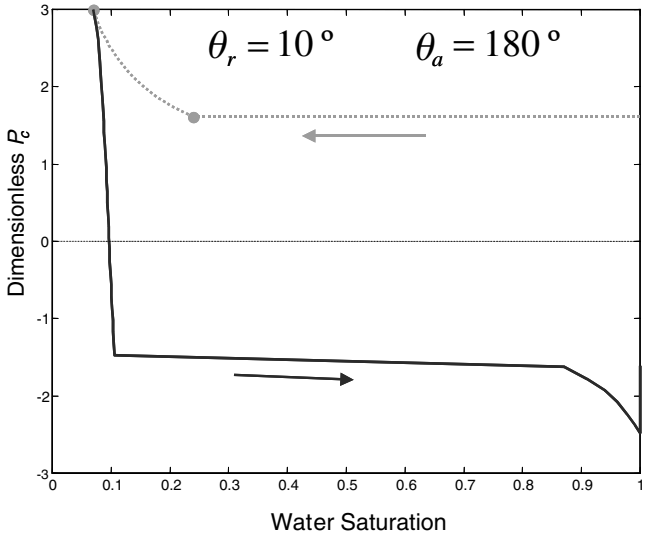

Fig. 24—The capillary pressures in drainage and piston-type imbibition of the triangular pore shown in Fig. 23. Note the nonlinear pore behavior and large capillary-pressure hysteresis resulting from the contact-angle hysteresis. The rightmost part of the imbibition curve follows the collapse of intermediate oil films.

ture for every I_2 event, depending on which two pore throats are involved. To simplify this procedure further, we may pick all the combinations of throat-radii pairs, each with a random weight, normalize them, and endow the average with a single weight:

$$\overline{R}_2 = \left[r_0 + w^{(2)} \frac{\sum_{j,k\ pairs} W_{jk}(r_j + r_k)}{\sum_{j,k} W_{jk}} \right] / \cos\theta_a, \quad \ldots\ldots\ldots\ldots (47)$$

where for each combination of throats j and k, W_{jk}=the uniform random weight between zero and one, and the normalizing factor in the denominator is the sum of the random weights. Now the common weight, $w^{(2)}$, is the relative importance given to the I_2 mechanism relative to the I_3 mechanism, and so on:

$$\overline{R}_n = \left[r_0 + w^{(n)} \frac{\sum_{n-touples} W_{jk\ldots n}(r_j + r_k + \ldots + r_n)}{\sum_{j,k\ldots n} W_{jk\ldots n}} \right] / \cos\theta_a. \quad \ldots (48)$$

The consecutive weights are found by numerical experimentation. The proposed model yields results similar to those of Blunt's model[22] with Øren *et al.'s* weights[10] when its weights are

$$w^{(2)}=0.72,\ w^{(3)}=0.45,\ w^{(4)}=1.2,\ w^{(5)}=1.5,\ w^{(n>5)}=5. \quad \ldots (49)$$

Fig. 25 compares the distribution of threshold capillary pressures for type I_4 events with those for piston-type invasion of the Bentheimer sandstone network. Note that the respective capillary pressures are lower than those for piston-type imbibition and the I_4 events are therefore less likely to occur.

Snap-Off. Snap-off is the invasion of an oil-filled pore by water AM's, which always exist in the corners of pore bodies and throats. If there is no contact-angle hysteresis, the AM's advance smoothly along the pore walls as the capillary pressure decreases. At a critical point, three of these AM's fuse together and become unstable; and the entire cross section of the pore fills with water, cutting the oil filament into two parts. The threshold capillary entry-pressure in piston-type imbibition is always higher that that for snap-off; therefore, snap-off occurs only when piston-type displacement is impossible for topological reasons (i.e., when there is no water/oil MTAM waiting at the pore end).

For a strongly water-wet system, the snap-off instability occurs at a threshold capillary pressure of

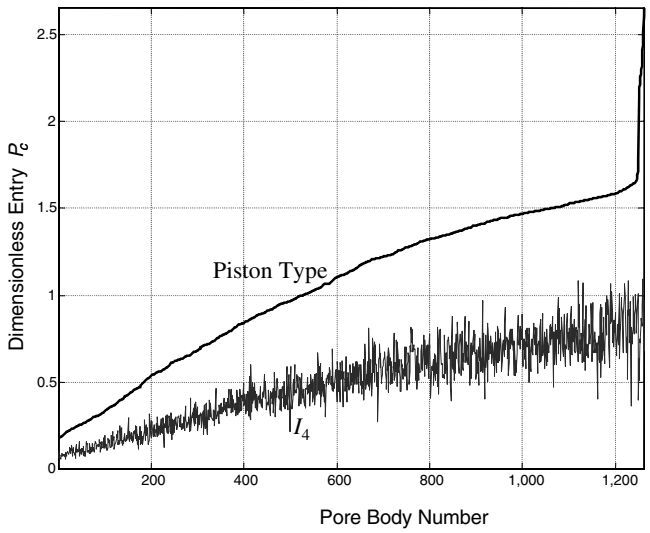

Fig. 25—The threshold capillary pressures for type I_4 cooperative pore-body filling sorted in order of the increasing corresponding piston-type threshold pressures. Note the stochastic noise introduced by the parametric model.

$$P^e_{c,SO} = \frac{\gamma_{ow}}{r}. \quad \ldots\ldots\ldots\ldots (50)$$

With contact-angle hysteresis, the AM's remain pinned at the positions established at the maximum capillary pressure in drainage, $P_{c,\max}$, until the hinging angle in the sharpest corner equals θ_a. Subsequent decrease of capillary pressure causes the sharpest corner's AM to advance towards the center of the pore. Eventually the advancing AM meets another one in the second sharpest corner (at the triangular pore base), causing snap-off. If $\theta_a<\pi/2+\min(\beta_i)$, the AM in the sharpest corner advances and merges with the other menisci at a positive capillary pressure. In this case, snap-off is spontaneous.

We calculate the threshold capillary entry-pressure for snap-off with contact-angle hysteresis, and $\theta_a<\pi/2+\min(\beta_i)=\pi/2+\min(\beta_i)$, by starting from the threshold capillary pressure in piston-type imbibition. Given the initial values of $r_{so}=r_p$ and $\theta_{h,i}$, obtained from Eqs. 38–41, we lower the capillary pressure gradually by increasing the meniscus radius and calculate the corresponding hinging angles, $\theta_{h,i}$, and the meniscus-to-vertex distances, b_i, from Eqs. 38 through 41. We then perform the following checks:

$$b_1(r_{so_1},\theta_{h,1})+b_2(r_{so_1},\theta_{h,2})<l_1=r\left(\cot\beta_1+\cot\beta_2\right), \quad \ldots\ldots\ldots\ldots (51)$$

$$b_2(r_{so_2},\theta_{h,2})+b_2(r_{so_2},\theta_{h,3})<l_2=r\left(\cot\beta_2+\cot\beta_3\right), \quad \ldots\ldots\ldots\ldots (52)$$

and

$$b_1(r_{so_3},\theta_{h,1})+b_3(r_{so_3},\theta_{h,3})<l_3=r\left(\cot\beta_1+\cot\beta_3\right), \quad \ldots\ldots\ldots\ldots (53)$$

where l_i=the lengths of triangle sides expressed through the inscribed circle radius and the corner half-angles. If one or more of conditions in Eqs. 51 through 53 is violated, two or three of the AM's have met and snap-off has occurred. Solving for the equality signs in each of the conditions in Eqs. 51 through 53, yields three different radii of the menisci, r_{so_i},i=1,2,3. The threshold capillary entry-pressure for snap-off occurs at the minimum radius (i.e., at the highest possible capillary pressure). Note that our procedure is somewhat different and more symmetric than that proposed in Ref. 10. Also, note that for $\theta_a=\pi/2-\beta_{\min}$ the threshold capillary entry-pressure for snap-off is zero (a flat meniscus in the sharpest corner advances). Therefore, in contrast to piston-type imbibition, spontaneous imbibition by snap-off occurs only for $\theta_a<\pi/2-\beta_{\min}$.

If $\theta_a>\pi/2-\min(\beta_i)=\pi/2-\beta_{\min}$, all three AM's are convex, their curvatures are negative and water invasion is forced. Once the hinging angle in the sharpest corner has increased to θ_a, its AM advances towards the center of the pore and the absolute value of its curvature decreases. This situation is analogous to the cause of instability of three concave menisci that meet. The convex AM is thus unstable and the part of the pore in which the instability has occurred immediately fills with water. The threshold pressure for this snap-off event depends on the curvature of the AM when it begins to move:

$$r_{so}\cos(\theta_a+\beta_{\min})=r_{pd}\cos(\theta_r+\beta_{\min}), \quad \ldots\ldots\ldots\ldots (54)$$

and the threshold capillary entry-pressure is given by

$$P^e_c = \frac{\gamma_{ow}}{r_{so}} = P_{c,\max}\frac{\cos(\theta_a+\beta_{\min})}{\cos(\theta_r+\beta_{\min})}, \quad \theta_a<\pi-\beta_{\min}. \quad \ldots\ldots (55)$$

Otherwise, the numerator in Eq. 55 is replaced by its smallest possible value ($\cos\pi=-1$) and

$$P^e_c = \frac{\gamma_{ow}}{r_{so}} = P_{c,\max}\frac{-1}{\cos(\theta_r+\beta_{\min})}, \quad \theta_a\ge\pi-\beta_{\min}. \quad \ldots\ldots (56)$$

Eq. 56 holds because the capillary entry-pressure vs. water saturation curve has a global minimum when $\theta_a+\beta_{\min}=\pi$. This minimum corresponds to the AM forming a half-circle. At higher water saturations, meniscus curvature decreases and the meniscus becomes

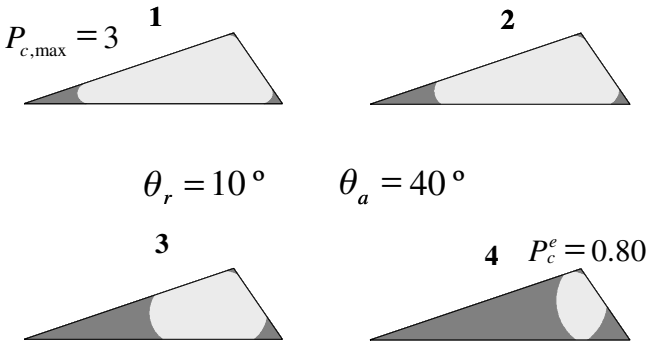

Fig. 26—Snap-off with contact-angle hysteresis. The AM in the widest corner remains pinned.

unstable.[23] For larger advancing contact angles, this unstable branch cannot be reached; hence, Eq. 56 comes into play.

Fig. 26 depicts snap-off with contact-angle hysteresis. The AM in the sharpest corner slides first, followed by the meniscus in the intermediate corner. The minuscule meniscus in the widest corner remains pinned; thus, the first two menisci touch resulting in snap-off.

The corresponding capillary pressures in the same pore are shown in **Fig. 27.** Because there is no MTAM waiting to invade, capillary pressure in imbibition falls to a low value, at which the two menisci in Fig. 26 touch, snap-off occurs and capillary pressure returns to its threshold value in drainage. As in piston-type imbibition, the pore behaves as a nonlinear valve with threshold and hysteresis.

Imbibition Results. The calculated capillary pressure curve in imbibition of the Bentheimer sandstone network is shown in **Fig. 28.** The calculated residual oil saturation to water is 31%. The correct calculation of relative permeabilities in imbibition is sufficiently involved to warrant a separate paper, and will be omitted here. However, agreement between the ANetSim and Statoil calculations of capillary pressure and relative permeabilities in concurrent imbibition is excellent.

Implementation

ANetSim has been implemented in MATLAB®[17] and runs on any platform with MATLAB installed on it. In particular, all the results presented in this paper have been obtained on a 266-MHz Dell Inspiron 3000 Notebook with 144 MB of memory. Most of the subroutines in ANetSim have been vectorized and take full advantage of vector- and matrix-handling capabilities of MATLAB. The CPU time for drainage and imbibition calculations on the Bentheimer sandstone network are shown in **Figs. 29 and 30.** The drainage calculations are quite competitive; it takes about 20 minutes to generate the full suite of calculations for the Bentheimer sandstone network.

The imbibition calculations are much slower (about 5 hours of CPU time) mostly because of time spent in a labeling subroutine that finds all clusters of the nonwetting phase connected to the outlet. This subroutine contains nested *if* statements, which disrupt MATLAB vectorization. In the future, the cluster subroutine will be rewritten in C and linked to the MATLAB code.

Conclusions

A quasistatic pore-network simulator, ANetSim, of two-phase drainage and imbibition has been written and verified against the state-of-the-art, proprietary simulator of Statoil. A complete description of all pore-level events has been incorporated. Pore-by-pore drainage- and imbibition-capillary pressure curves, including their unstable branches, have been obtained. ANetSim predicts successfully the absolute rock permeability, and the relative permeabilities in primary and higher-order drainage processes. Secondary and higher-order imbibition relative permeabilities are also predicted. The simulator predictions are in good agreement with Statoil's calculations and experiments. Thus, quasistatic pore-network simulators can be used in quantitative predictions of fluid transport in permeable rocks. Image analysis must be used to convert the imaged pore-space geometry into an equivalent pore network.

The rule-based pore-network simulators with complete physics of quasistatic drainage and imbibition are still rare. ANetSim, in particular, has the following features:

1. Arbitrary triangular, rectangular, and elliptic cross sections of pore bodies (nodes) and throats (links).
2. Arbitrary spatial distribution of connectivity between nodes and links.
3. Arbitrary distribution of rock wettability captured by the variable receding and advancing contact-angles.
4. Corner-filament flow with arbitrary contact-angle hysteresis.
5. Piston-type displacement and snap-off with arbitrary contact angles and for arbitrary conditions after primary drainage.
6. Cooperative pore-body filling (I_n mechanisms).
7. Models of spatial distribution of altered wettability.
8. Efficient oil-cluster checking algorithm.
9. Efficient pore-by-pore invasion percolation algorithm with all site and bond-breaking mechanisms.

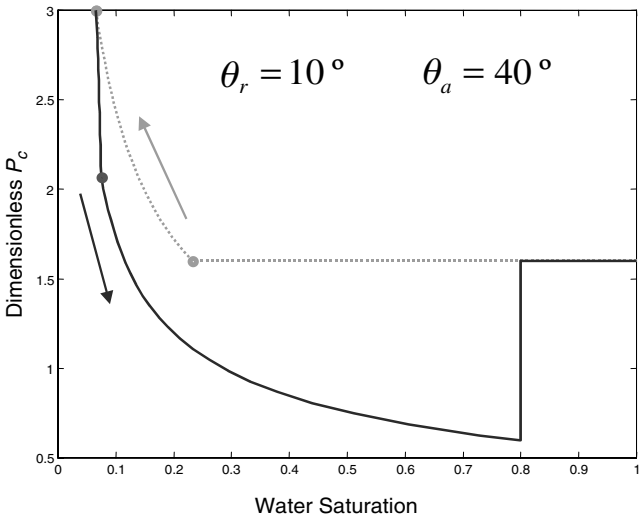

Fig. 27—Capillary-pressure curves in drainage and imbibition with snap-off shown in Fig. 26. The pressure jump is caused by the menisci merging at , snap-off occurring and the pore pressure returning to the capillary entry pressure level.[25]

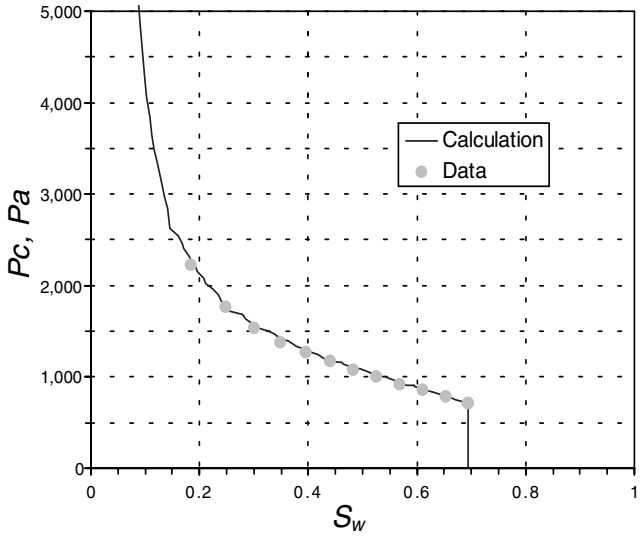

Fig. 28—The capillary-pressure curve in imbibition of the Bentheimer sandstone network. The points denote the Statoil calculations.

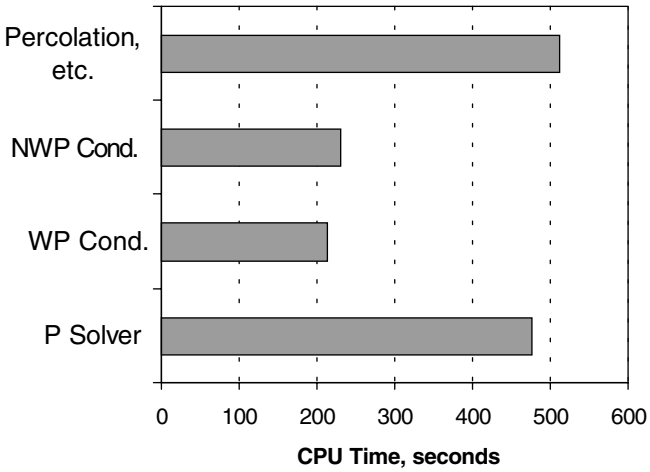

Fig. 29—CPU time for the Bentheimer sandstone drainage calculations on a 266-MHz Dell Inspiron 3000 Notebook with MATLAB 5.2.1 and Windows NT 4.0/SP 5. Note that the pressure solver is very competitive with the compiled C or FORTRAN programs. NWP cond. = the calculation of the nonwetting-phase hydraulic conductances, etc.

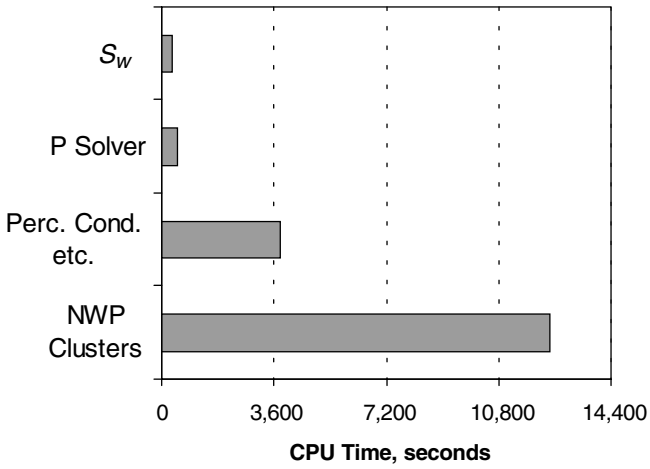

Fig. 30—CPU time for the Bentheimer sandstone imbibition calculations on a 266-MHz Dell Inspiron 3000 Notebook with MATLAB 5.2.1 and Windows NT 4.0/SP 5. Note that the majority of CPU time is spent on determining the nonwetting-phase cluster connectivity to the outlet. Perc. Cond. etc., = the imbibition percolation algorithm, the calculation of hydraulic conductances, and the setup of the pressure equations for each phase.

In return, ANetSim can calculate:

1. Full capillary-pressure curves under primary drainage and secondary imbibition.
2. Higher-order capillary-pressure scanning loops.
3. Relative permeabilities under the respective drainage and imbibition loops.
4. Residual nonwetting-phase saturation, and
5. Formation resistivity factor.

Nomenclature

a = constant in the quadratic correlation of the dimensionless hydraulic conductance factor
b = pore vertex-corner meniscus distance, m
C_l = constant defined in Eq. 36
F = pore-shape function in drainage
g = hydraulic conductance, m^2/Pa-s
$\bar{g}_w$ = dimensionless hydraulic conductance
$\tilde{g}_w$ = scaled dimensionless hydraulic conductance of water filament
G = Morrow's shape factor
$\tilde{G}$ = shape factor of single corner filament
I_n = cooperative pore-body filling events with n throats occupied by oil
k = intrinsic or absolute permeability, m^2
l = length of pore channel, m
N = number of network nodes
p = single-phase pressure, Pa
P = pore cross-section perimeter, m
P_c = capillary pressure, Pa
q = volumetric flow rate
r = inscribed circle radius, m
$\overline{R}$ = mean radius of curvature, m
R = flow resistance, Pa·s/m
S = fluid saturation
t = tangent of the corner half-angle
V = volume, m
w = weight factor
W = random weight factor
α = half-angle subtended by meniscus arc relative to its center of curvature, rad
$\boldsymbol{\alpha}$ = expansion constant
β = pore corner half-angle, rad
δ = expansion constant
χ = dimensionless resistance factor
φ = porosity, fraction
γ = interfacial tension, N/m
μ = bulk viscosity, Pa·s
θ = contact angle, rad

Subscripts/Superscripts

a = advancing
b = body (of pore)
c = capillary
d = drainage
e = entry
h = hinging
i, IJ = flow of phase i in the flow unit IJ .
j, k = represent n-touples of pore throats connected to a pore body
max = maximum capillary pressure in primary drainage
n = number of oil-filled throats
o = oil or nonwetting phase
ow = oil/water
p = pore or corresponding to capillary-pressure level in imbibition
PD = primary drainage
PT = piston type
r = receding
so, SO = snap-off
t = throat (of pore)
w = water

Acknowledgments

I would like to thank Dr. Paal-Eric Øren of Statoil for hosting me in Trondheim, Norway, during the Fall 1998 sabbatical leave from U. of California, Berkeley, and for helping in the development and debugging of my pore-network simulator. I would like to thank all three reviewers for their extensive and very helpful remarks. This work was sponsored in parts by Statoil, U.C. Berkeley, and PV Technologies, Inc.

References

1. Morrison, P. *et al.: Powers of Ten*, Scientific American Library, New York City (1982) 150.
2. *Lattice Gas Methods for Partial Differential Equations*, G.D. Doolen (ed.), The Advanced Book Program, Addison-Wesley Co., Redwood City, California (1990).

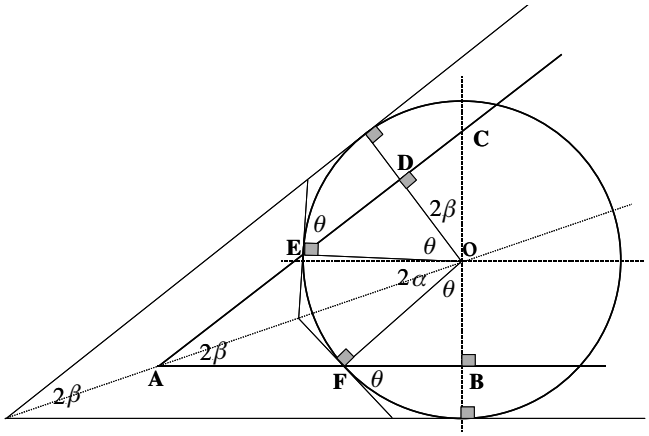

Fig. 31—Corner-filament geometry.

3. Xu, B. *et al.:* "Use of Pore-Network Models to Simulate Laboratory Corefloods in a Heterogeneous Carbonate Sample," *SPEJ* (September 1999) 179.
4. Gaylord, R.J. and Wellin, P.R.: *Computer Simulations With Mathematica-Explorations in Complex Physical and Biological Systems,* The Electronic Library of Science, Springer Verlag, Santa Clara, California (1995).
5. DeGennes, P.G.: "Percolation: A New Unifying Concept," *La Recherche* (1980) 7, 919.
6. Wilkinson, D. and Williamsen, J.F.: "Invasion Percolation: A New Form of Percolation Theory," *J. Phys. A: Math. Gen.* (1983) **16,** 3365.
7. Dias, M.M. and Wilkinson, D.: "Percolation With Trapping," *J. Phys. A: Math. Gen.* (1986) **19,** 3131.
8. Lenormand, R., Zarcone, C., and Sarr, A.: "Mechanisms of Displacement of One Fluid by Another in a Network of Capillary Ducts," *J. Fluid Mech.* (1983) **135,** 337.
9. Lenormand, R.: "Pattern Growth and Fluid Displacements Through Porous Media," *Physica A* (1986) **140,** 114.
10. Øren, P.-E., Bakke, S., and Arntzen, O.J.: "Extending Predictive Capabilities to Network Models," *SPEJ* (December 1998) 324.
11. Patzek, T.W.: *E240-Fundamentals of Multiphase Flow in Porous Media,* first edition, U. of California at Berkeley, Berkeley, California (1999) 250.
12. Mason, G. and Morrow, N.R.: "Capillary Behavior of a Perfectly Wetting Liquid in Irregular Triangular Tubes," *J. Colloid and Interface Sci.* (1991) **141,** 262.
13. Patzek, T.W. and Silin, D.B.: "Shape Factor and Hydraulic Conductance in Noncircular Capillaries: I. One-Phase Creeping Flow," *J. Colloid and Interface Sci.* (2001) **236,** 295.
14. Patzek, T.W. and Kristensen, J.G.: "Shape Factor and Hydraulic Conductance in Noncircular Capillaries: II. Two-Phase Creeping Flow," *J. Colloid and Interface Sci.* (2001) **236,** 305.
15. Ransohoff, T.C. and Radke, C.J.: "Laminar Flow of a Wetting Liquid Along Corners of a Predominantly Gas-Occupied Non-Circular Pore," *J. Colloid and Interface Sci.* (1987) **121,** No. 2, 392.
16. Kristensen, J.G.: *The Universal Scaling of Conductance in Laminar Film Flow of Wetting Liquid Along the Corners of An Angular Pore,* U. of California at Berkeley, Berkeley, California (1999).
17. Mathworks: *MATLAB-The Language of Technical Computing,* Mathworks, Inc., Natick, Massachusetts (1998).
18. Mayer, R.P. and Stowe, R.A.: "Mercury-Porosimetry Breakthrough Pressure for Penetration Between Packed Spheres," *J. Colloid and Interface Sci.* (1965) **30,** 893.
19. Princen, H.M.: "Capillary Phenomena in Assemblies of Parallel Cylinders. I. Capillary Rise Between Two Cylinders," *J. Colloid and Interface Sci* (1969) **30,** 60.
20. Princen, H.M.: "Capillary Phenomena in Assemblies of Parallel Cylinders. II. Capillary Rise in Systems With More Than Two Cylinders," *J. Colloid and Interface Sci.* (1969) **30,** 359.
21. Princen, H.M.: "Capillary Phenomena in Assemblies of Parallel Cylinders. III. Liquid Columns Between Horizontal Parallel Cylinders," *J. Colloid and Interface Sci.* (1970) **34,** 171.
22. Blunt, M.J.: "Pore Level Modeling of the Effects of Wettability," *SPEJ* (December 1997) 449.
23. Brown, R.A.: *The Shape and Stability of Three Dimensional Interfaces,* U. of Minnesota, Minneapolis, Minnesota (1979).
24. Patzek, T.W.: "AmSim-Single Pore Meniscus Equilibria Simulator," U. of California at Berkeley, Berkeley, California (1998).
25. Ma, S., Mason, G., and Morrow, N.R.: "Effect of Contact Angle on Drainage and Imbibition in Regular Polygonal Tubes," *Colloids and Surfaces A: Physicochemical and Engineering Aspects* (1996) **117,** 273.

Appendix

The geometry of the corner-water filament is shown in **Fig. 31.** In particular, twice the corner half-angle $2\beta = \angle BAD$; the contact angle $\theta = \angle AEH = \angle IED$ twice the half-angle subtended by the meniscus $2\alpha = \angle EOF = \pi - 2\beta - 2\theta$; the meniscus-apex distance $b = AF$ and the meniscus radius is $r_p = OE$.

SI Metric Conversion Factors

ft × 3.048*	E − 01 = m
in. × 2.54*	E + 00 = cm
psi × 6.894 757	E + 03 = kPa
bar × 1.0*	E + 05 = Pa

*Conversion factor is exact

Tad W. Patzek is an associate professor of GeoEngineering at the Dept. of Civil and Environmental Engineering, U. of California, Berkeley. e-mail: patzek@patzek.berkeley.edu. Prior to joining Berkeley, he was a senior reservoir engineer at Shell Western E&P Inc. (1989–90); senior research engineer (1986–89) and research engineer (1983–86) at the Enhanced Recovery Research Dept., Shell Development; research associate at the Chemical Engineering Dept., U. of Minnesota (1981–83); and research associate at Chemical Engineering Research Center, Polish Academy of Sciences, Gliwice, Poland. Patzek has authored 90 papers, 38 industrial reports, and 15 expert witness reports and depositions. In 1995, Patzek was a Distinguished Lecturer for SPE, and he is a member of the SPE Speakers Bureau.